An experimental investigation on damage mechanisms of thick hybrid composite structures under flexural loading using multi-instrument measurements

S. Gul [a,b,c], I.E. Tabrizi [a,b,c], B.S. Okan [a,b,c], A. Kefal [a,b,c,*], M. Yildiz [a,b,c]

[a] Integrated Manufacturing Technologies Research and Application Center, Sabanci University, Tuzla, Istanbul 34956, Turkey
[b] Faculty of Engineering and Natural Sciences, Sabanci University, Tuzla, Istanbul 34956, Turkey
[c] Composite Technologies Center of Excellence, Istanbul Technology Development Zone, Sabanci University-Kordsa Global, Pendik, Istanbul 34906, Turkey

ARTICLE INFO

ABSTRACT

In this study, damage characterization of thick carbon/glass fiber reinforced hybrid composites is performed under flexural loading conditions via two non-destructive evaluation (NDE) techniques, i.e., digital image correlation (DIC) and acoustic emission (AE). Experimental results demonstrate that the flexural modulus of the hybrid composites is strongly correlated with the location of carbon fiber plies; the closer these plies are to the laminate faces, the higher is the modulus. On the other hand, the flexural strength depends on the type and extent of damage initiation in the laminates. Interply hybridization of carbon fiber reinforced composites (CFRPs) with glass fiber not only improves their flexural strength and failure strain but also facilitates failure predictability in CFRPs. The transverse and shear strains associated with various failure modes in thick hybrid laminates are efficiently captured by the DIC technique. In addition, AE results reveal that the strain levels associated with the onset of acoustic activity are linked to failure in the carbon fiber plies of the hybrid laminates. Furthermore, these observations made by DIC and AE on thick hybrid laminates are confirmed with optical fractography. Finally, it is revealed that ply lay-up sequence and laminate thickness notably alter both the mechanical performance and damage mechanisms of hybrid composites.

© 2021 Elsevier Masson SAS. All rights reserved.

1. Introduction

Carbon fiber reinforced polymer composites (CFRPs) are widely used in high-performance engineering applications due to their high strength to weight ratio, significant fatigue strength, chemical resistance, and dimensional stability. CFRPs can offer considerable weight reductions compared to their conventional metallic counterparts, especially in automotive and aerospace applications [1]; for example, Boeing 787 Dreamliner's airframe is 50% advanced composite by mass [2]. However, despite their many merits, engineering structures based on CFRPs are prone to stress concentrations and growth of breakage clusters around the broken carbon fibers [3,4]. Gradual/cyclic accumulation of micro-cracks in CFRPs can lead to poor residual strength of the material, ultimately leading to sudden catastrophic failure of the primary structural components.

To mitigate the abrupt stiffness loss shown by CFRPs, various techniques ranging from the manufacturing of variable stiffness laminates [5,6] to the use of nano-/micro-sized reinforcements have been considered. For example, nano-silica/rubber microparticles were added to an epoxy matrix of fiber-reinforced composites by Hsieh et al. [7]. The prepared epoxy polymer improved the fracture delamination energy of composites through the mechanisms of fiber bridging and fiber debonding. Similarly, Wong et al. utilized a toughening method based on dissolvable chopped thermoplastic fibers in a carbon fiber epoxy composite [8]. These fibers were added at the interlaminar regions, and upon heating formed a second phase within the resin, thus improving the mode-I fracture toughness of CFRPs by 10 times. A method based on carbon nanotube reinforcement was used by Kepple et al. to enhance the damage tolerance of CFRPs. The resulting structure had an improved flexural modulus and better resistance to delamination [9]. AlKhateab et al. also used nanostructures to prepare CFRPs reinforced with halloysite nanotubes (HNTs) and enhanced the in-plane and shear moduli of laminates by 27% and 18%, respectively [10]. The addition of HNTs improved matrix cracking and debonding mechanisms and significantly reduced the extent

of damage accumulation in composite specimens. Although all of these techniques are promising to modify the mechanical behavior of CFRPs, they are primarily focused on the improvement of matrix-dominated properties and present scalability limitations.

An alternative economical and scalable technique to improve the low toughness and failure strain of CFRPs is 'interply fiber hybridization'. In this method, a hybrid fiber-reinforced laminate is obtained by stacking plies of two or more types of fibers in a special layup arrangement, usually in a single resin system. Thus, a material can be designed having combined benefits of the individual components, while diminishing their disadvantages. Among the available hybridization candidates for CFRPs [11–13], glass fibers have elicited the attention of researchers due to their ductility, good fracture toughness, and comparatively lower cost [14,15]. One of the important properties achieved in carbon/glass fiber hybrid composites is the enhancement of failure strain compared to the non-hybrid carbon composites [16]. A modeling study conducted by Swolfs et al. [17] proposed that interply hybridization of a composite with a well-designed layer sequence not only provides a positive hybrid effect but also reduces the number of pathways for failure growth by efficiently delaying the development of break-clusters. Similar observations regarding changes in failure response of hybridized CFRPs under high-velocity impacts were recorded by M. Mousavi [18]. They observed that on replacing the back carbon layers with glass/Kevlar fibers, energy absorption of the laminate can be improved by 23%. Dong et al. [19] studied the effect of various stacking sequences, fiber volume fractions, and span-to-thickness ratios on the mechanical properties of carbon/glass hybrid composites. In their prepared thin-ply laminates, it was observed that the higher the volume fraction of glass fiber plies is, the greater the flexural strength will be. Furthermore, Prusty et al. [20] suggested that the characteristic brittle failure of CFRPs under loading can be avoided by using a stacking sequence where glass fibers are available on the tensile side of the specimen. Similarly, the tensile behavior of carbon/glass fiber hybrid laminates was discussed in detail by Tabrizi et al. [21]. Premature failure of carbon layers was prevented by using glass layers between carbon plies, thereby achieving a significant improvement in tensile strength through the hybridization of laminates. Additionally, the thermal conductivity difference between carbon and glass layers can lead to high compressive residual stresses during hybrid composite manufacturing. These stresses subsequently favor the increase in tensile strength of the hybrid specimens as compared to the classical CFRP laminates. Hence, careful placement of the carbon or glass plies through the thickness of the laminate can play an important role in tailoring the overall mechanical properties and damage response of a hybrid laminate.

As composite materials find their way towards applications in primary and secondary load-bearing structures e.g., wing covers of Airbus A350 XWB, their thickness has increased significantly. Generally, any laminate with a thickness ≥ 6 mm can be considered as a 'thick' composite structure [22–25]. However, from a mechanical modeling point of view, the thick laminates are classified based on a span-to-thickness ratio of less than 20. In the literature, the majority of the investigations discussing the relationship between layer sequence and mechanical properties of interply hybridized composites deal with thin laminates. Moreover, studies available on thick laminates are primarily focused on non-hybrid CFRPs/GFRPs [26–28]. As the damage manifestation in thick laminates is highly localized, it is characteristically different from the crack-growth behavior observed in the thin-ply composites [29,30]. Increased laminate thickness also contributes to an upsurge in the interlaminar shear stress values and their distribution, ultimately leading to delamination failure in thick laminates [31]. In this context, a thorough understanding of damage characterization in hybridized thick laminates would be a crucial step in the design of future composite materials for use in aeronautical and maritime structures. A unique opportunity where a laminate is subjected to a simultaneous application of tensile, compression, and shear stresses can be provided by a flexural test e.g., a 3-point bending test [32]. Additionally, during this type of mechanical loading, the well-defined localization of the damage can be efficiently captured by using commonly available non-destructive evaluation (NDE) and structural health monitoring (SHM) techniques. For example, shape sensing and SHM methods have been utilized together with strain sensors to monitor structural deformations and stresses of aircraft structures with variable cross-sections [33] and complex blade-stiffened topologies [34]. In addition, during the last couple of decades, NDE methods including acoustic emission (AE), infrared thermography (IR), X-ray computed tomography (CT), and digital image correlation (DIC) have become indispensable to the in-service inspection of composite materials and damage analysis of engineering structures.

DIC is an optical technique used for the two-/three-dimensional full-field displacement and strain monitoring of a deforming and/or displacing material [35,36]. During the test, a high-resolution single/stereo camera is used to record a series of digital images of a sample surface having a speckle pattern. The images are later converted to grayscale and treated as a matrix whereby each element corresponds to a pixel representing a specific point on the specimen surface. A correlation algorithm is used to compare the consecutive images taken from the surface during deformation, and the spatial displacement fields are computed accordingly. For example, recently, DIC method was used for reliable full-field strain measurements of a very-light airplane (VLA) by A. Pagani et al. [37]. Although DIC is a readily applicable optical method without requiring a complex surface treatment [38], the measurement accuracy of the DIC technique can be affected by factors like camera lens distortion or quality of speckle pattern [39]. Therefore, to better understand the damage development and failure stages under various loading conditions, a viable non-optical NDE method such as acoustic emission needs to be paired with DIC.

During mechanical loading, microdamage initiation and growth in the material cause dissipation of the strain energy in the form of acoustic waves, which propagate throughout the material. These waveforms can be collected by surface-mounted piezoelectric sensors and converted to electrical signals. The recorded electrical signals are processed by an appropriate data processing equipment to extract the features of each single acoustic emission wave. As the composite materials exhibit a multiplicity of energy dissipative processes such as fiber-matrix debonding, matrix fracture, fiber breakage, and fiber pull out, AE waveform features (e.g., amplitude distribution, counts, duration to failure) can be used to efficiently identify these damage events [40–42]. Though AE is an important *in-situ* structural health monitoring technique, its capabilities are limited in terms of providing strain evolution during the deformation of composite specimens.

The presence of multiple failure modes, possible simultaneous initiation of two or more failure modes, and complex stress states in a specimen under a flexural load necessitates the use of a multi-instrument approach [43–47]. Oz et al. employed a simultaneous application of the DIC and AE technique to predict the formation of surface cracks due to emitted stress waves in a CFRP specimen [48]. Similarly, Cuadra et al. [43] utilized a hybrid system consisting of AE-DIC-IR techniques for the investigation of damage accumulation in a glass fiber reinforced laminate. Information about stiffness degradation, energy dissipation, and the influence of fatigue cycles on average strain was effectively extracted during mechanical testing. The full-field strain maps revealed the development of damage 'hot-spots' in the GFRP under uniaxial loading, which correlated well with the recorded acoustic activities. Similarly, the damage progression profile of patch-repaired GFRP
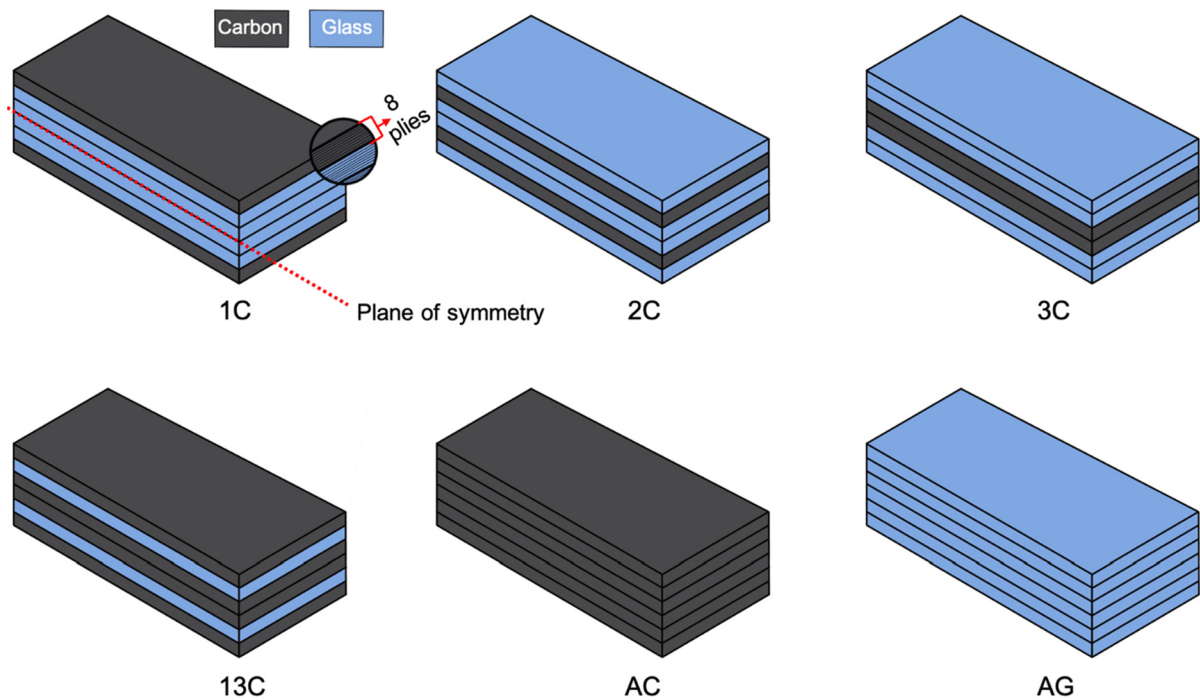
Fig. 1. Schematic of stacking sequence used for manufacturing of composite laminates.

laminates was assessed using a hybrid AE-DIC method by Andrew et al. [45]. They concluded that the AE data demonstrate distinct damage zones for a specimen under compression test associated with the detection of first permanent damage, the occurrence of macroscopic failure, unstable damage growth, and global failure. DIC was used to obtain the average full-field strain measurements at these marked zones in the AE count versus time graph. Recently, damage analysis of CFRPs under tensile and flexural loading conditions was performed by correlating the DIC and AE methods by Ali et al. [49]. The fractography of the failed specimens was directly compared to the strain fields of the samples obtained by a 3D-DIC system at failure regions. The proposed clustering method effectively classified various failure modes including matrix cracking, delamination failure, and fiber breakages in the composite laminates during mechanical loading. Hence, the cross-validation of data obtained from various techniques not only helps in achieving an effective understanding of failure evolution in composite materials but also improves the reliability of each monitoring method.

Despite the availability of numerous studies on the use of multi-instrument NDEs for damage analysis of composites, the application of these techniques to quantify the damage accumulation and propagation in thick hybrid composites is still understudied [23]. In this regard, the main aim of the current study is to experimentally investigate the flexural response of a thick carbon/glass hybrid laminate as a function of its stacking sequence. Moreover, two non-destructive evaluation techniques, namely acoustic emission, and digital image correlation are used for the qualitative and quantitative assessment of damage modes exhibited by composite specimens during a 3-point bending test. To the best of the authors' knowledge, the present research is the first investigation that uses a multi-instrument approach for failure analysis of thick hybrid laminates under flexural loading conditions. In addition, it provides a detailed comparison of damage mechanisms between thick hybrid laminates and thin hybrid laminates previously studied in [21].

In the forthcoming parts of this study, Section 2 describes the fabrication process of thick composite laminates, details of the mechanical test setup, digital image correlation technique, acous-

tic emission monitoring setup, and fractography methods. In Section 3, the results of the flexural tests and damage mechanisms demonstrated by the laminates, full-field strain measurements using DIC, and prediction of damage accumulation via the AE method are presented. Section 4 includes the concluding remarks regarding various observations of the current study.

2. Materials & methods

2.1. Composite specimen manufacturing

Unidirectional prepreg comprising of carbon fibers and epoxy resin is purchased from Kordsa Teknik Tekstil A.S. (Turkey) with the product code of KOM10 34700 HTCF UD300 37% 600KOMP. The areal weight of carbon prepreg is 300 g/m^2 and the resin content is 37 wt%. Moreover, unidirectional E-glass fiber prepreg with epoxy resin is also acquired from Kordsa Teknik Tekstil A.S. (Turkey) with the product code of KOM10 WR6 2400TEX EGF UD300 35% 600KOMP. The glass prepreg has an areal weight of 300 g/m^2 and the resin content is 35 wt%. The carbon fiber and glass fiber prepregs are cut into dimensions of 300 × 300 mm using a ply cutter (ZÜND G3-L3200) and 48 layers of prepregs are stacked upon each other in a unidirectional configuration. Non-hybrid specimens, used as reference materials with a configuration of $[C_{48}]$ and $[G_{48}]$, are named as AC and AG, respectively. Four symmetric layup sequences $[C_8/G_8/G_8]_s$, $[G_8/C_8/G_8]_s$, $[G_8/G_8/C_8]_s$ and $[C_8/G_8/C_8]_s$ are used for hybrid specimens, and the configurations are named as 1C, 2C, 3C, and 13C, respectively. Fig. 1 shows the stacking sequences used to manufacture the laminates.

A steel mold is thoroughly cleaned with ethanol. Afterward, three layers of both the sealing agent (XTEND 838) and releasing agent (XTEND CX-500) are applied to the surface of the steel mold, with a 15 min interval between each application to allow their proper functioning. Afterward, the stacked prepregs are placed onto the prepared steel mold. A manual hot press (MSE Teknoloji Ltd.) is used to cure the prepregs. According to the technical data sheet provided by the prepreg manufacturer the steps
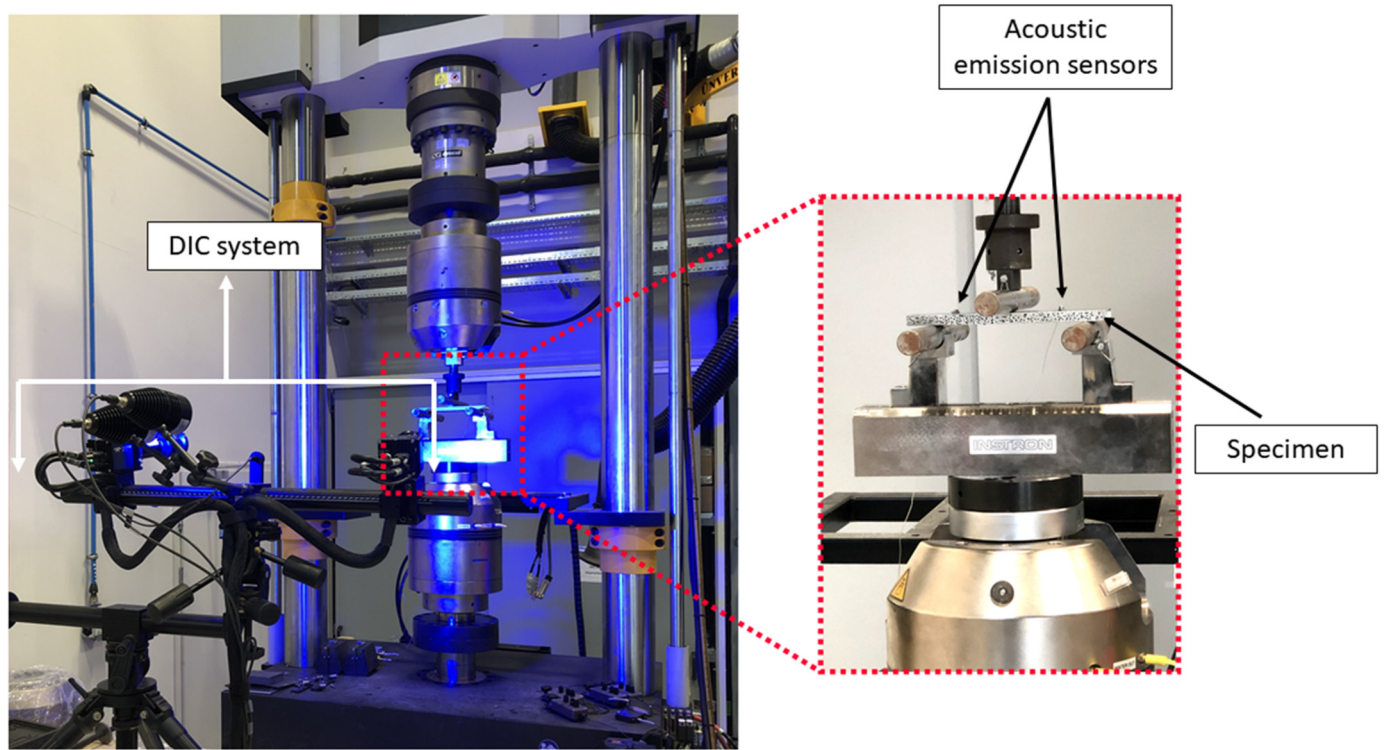
Fig. 2. Flexural test with DIC system for through-thickness strain measurements and AE sensors mounted on the specimen.

followed for curing of the matrix are: (i) initially, the hot press is heated to 20 °C (ii) temperature is increased to 120 °C at a heating rate of 2–3 °C/min, while the pressure is gradually increased to 6.4 bars (iii) temperature and pressure are maintained at 120 °C and 6.4 bars, respectively for 60 min (iv) after curing, a cooling rate −2 °C/min is used to lower the temperature to 80 °C before releasing the pressure (v) the laminate is allowed to cool to the room temperature before demolding.

2.2. Experimental setup

For 3-point bending tests, samples in the fiber direction of laminates (0°) are cut according to dimensions mentioned in ASTM D790-A standard [50] using a water-jet machine (KUKA KR16 F). Tests are conducted on Instron® 5982 Universal Testing Machine with a 250 kN load cell. An average crosshead speed of 5 mm/min is used during the tests. The support span length to thickness ratio (L/d) is kept 16:1 for all samples. According to the ASTM D790-A standard, the following formulas for the computation of flexural stress (σ) and flexural strain (ε) are used:

$$\sigma = \frac{3PL}{2bd^2} \tag{1}$$

$$\varepsilon = \frac{6Dd}{L^2} \tag{2}$$

Where P is the load at a given point on the load-displacement curve. L, b, and d is the support span, specimen width, and specimen depth, respectively, while D is the maximum deflection measured at the center of the specimen. Table 1 provides the specimen dimensions used for bending tests.

To obtain the full-field strain maps along the span length of bending specimens, a digital image correlation (DIC) technique with GOM (Braunschweig, Germany) 12M sensor system is used. Using black and white spray paints, a speckle pattern is generated on the specimens as shown in Fig. 2. Calibration of the DIC instrument is performed using a 250×200 mm² calibration object

Table 1
Specimen dimensions [mm] for the 3-point bending tests.

Sample	Support span	Depth	Width
AG	171	10.70	46.28
1C	170	10.70	42.08
2C	180	11.33	45.35
3C	190	11.85	45.40
13C	200	12.46	48.05
AC	224	14.00	53.33

according to the manufacturer's directions. With the ARAMIS® professional software, the surface pattern quality is inspected before starting the mechanical tests to ensure the presence of a proper grayscale contrast to be monitored by the DIC camera. For identification of the surface of interest for DIC software and subsequent correlation of the surface points with different grayscale during the deformation, facets of the size of 25×25 pixels, and step size of 19×19 pixels are defined for the DIC software. By using ARAMIS® software, the in-plane displacement of surface facets during the flexural tests is correlated and a full field displacement/strain maps of the specimens are obtained as a result.

The Acoustic Emission (AE) technique is used to monitor damage evolution during the bending tests. Detection of the elastic acoustic waves (hits) generated due to micro-damage is done by two piezoelectric sensors (PICO-2-750 kHz Lightweight Miniature AE sensors, Mistras) attached to the top layer of bending specimens using a hot-glue gun, as shown in Fig. 2. Both sensors are 60 mm apart and equidistant from the center of the specimen, and a sensitivity threshold of 45 dB is set to record the input hits. Amplification of the signal outputs from the sensors is done using a preamplifier which imposes a 20-dB gain to recorded acoustic emission waves. A Bessel band-pass filter with a range of 20–800 kHz is used to eliminate the noise from acquired signals using NEOSIS® software, and Fast Fourier Transform (FFT) is performed to extract frequency domain features like peak frequency, partial power, frequency centroid, etc. for each acoustic hit.
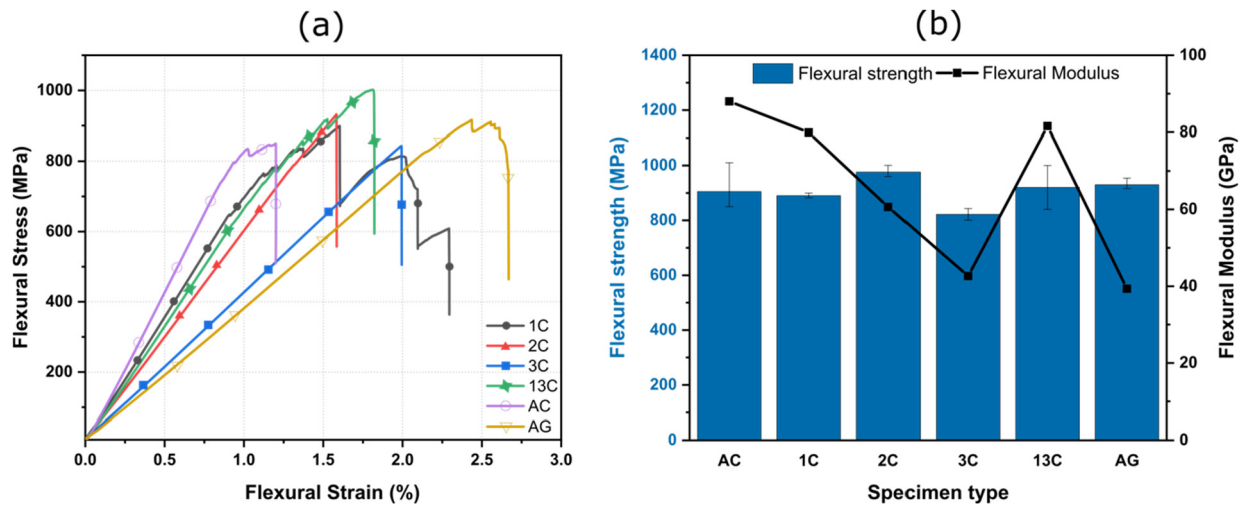
Fig. 3. (a) Flexural stress–strain curves for composite laminates, (b) Flexural modulus and flexural strength of laminates.

The optimum number of clusters for the acoustic emission data is found to be three, based on the K-means algorithm used with the Davies–Bouldin dissimilarity function. Moreover, clustering of acoustic emission data for each sample is based on two extracted features namely, weighted peak frequency (WPF) and partial power 1% (PP1), which have previously shown to provide well-defined clustering results [44,51,52]. In this study, PP1 % defines the percentage of signal power located in a frequency range of 0–200 kHz. Weighted peak frequency is a function of frequency centroid and peak frequency. The center of the mass for the spectral range of recorded acoustic emission signal in frequency domain is the frequency centroid, while the Fast Fourier Transformation of the time domain signal provides the peak frequency. WPF is calculated using the following formula:

$$\text{WPF} = \sqrt{\text{Frequency centroid} \times \text{Peak frequency}} \qquad (3)$$

The fractography of the failed specimens is performed using a Nikon LV 100 ND stereo optical microscope and Leo Supra35VP field emission scanning electron microscope (SEM). Samples for SEM characterization are prepared using a precise diamond cut-off machine (Struers Discotom-10) and the fractured surfaces are sputter-coated with a thin layer of gold before investigation.

3. Experimental results

3.1. Flexural behavior and predictability of failure path for hybrid laminates

The experimental results of 3-point bending tests are presented in Fig. 3(a), showing the evolution of stress versus strain for the non-hybrid (AC, AG) and hybrid (1C, 2C, 3C, 13C) specimens. As all the samples of a particular stacking sequence exhibited similar stress–strain behavior during the bending test, a specimen with an average strength is chosen for each laminate as shown in Fig. 3(a). As per the ASTM D790-A standard, stress values are calculated using the load cell data, while strains are calculated using deflection at the center of specimens during the bending test. The flexural modulus is calculated as chord modulus between the strain range of 1000 $\mu\varepsilon$–3000 $\mu\varepsilon$ in the stress–strain curve according to ASTM D790-A standard.

A close inspection of σ–ε curves in Fig. 3(a) reveals the linear elastic region for all specimens. However, strain values corresponding to the deviation point from the elastic region are strongly dependent on the stacking sequence used for the hybrid specimens.

Table 2
Flexural properties of composites laminates.

Sample	Flexural strength (MPa)	Flexural modulus (GPa)	Strain to global failure (%)
AC	905	87.99	1.21
1C	890	79.95	2.29
2C	976	60.62	1.58
3C	822	42.66	1.99
13C	920	81.60	1.81
AG	930	39.35	2.66

The lowest failure strain i.e., 1.2%, is observed for the AC specimen due to the high stiffness of carbon fibers. However, an improvement of strain at failure value ($\varepsilon_{failure}$) of AC specimen is attained upon interply hybridization of AC specimen by replacing some of the carbon layers with the glass ones. For example, 1C specimen presents an improvement of 1.9 folds in $\varepsilon_{failure}$ as compared to AC. This improvement can be attributed to the replacement of carbon plies located along the horizontal midplane with the glass fiber (having smaller stiffness) in the 1C laminate. The highest failure strain is observed for the AG specimen, as the glass fibers have higher relative ductility and provide a comparatively efficient load transfer between plies during loading [53,54].

On the other hand, the highest flexural modulus is observed for the AC specimen, while an apparent trend in reduction of flexural modulus is captured for the hybrid specimens with similar relative volume fraction of carbon to glass fibers, namely 1C, 2C, and 3C. Such reduction is caused by moving the carbon plies away from the faces and towards the horizontal midplane of the specimens. It is also observed that the flexural modulus values of 1C and 13C specimens are very similar since both laminates have carbon plies on the bounding top and bottom surfaces of the laminate that are being subjected to maximum compressive and tensile stresses during flexural loading. Therefore, the initial flexural stress–strain behavior in hybrid laminates can be directly controlled by altering the relative location of high stiffness plies with respect to the neutral plane under bending loading condition. In Fig. 3(b), the average flexural strength of 1C, 2C, and 3C hybrid specimens are varying, although they contain similar amounts of carbon and glass fiber plies, thereby indicating that the flexural strength does not have a direct dependence on the stacking sequence of specimens.

To make a more quantitative comparison between the composite specimens, their flexural properties are listed in Table 2. The 2C specimen exhibits the highest strength value, i.e., 976 MPa, while the lowest strength is exhibited by the 3C specimen as illustrated
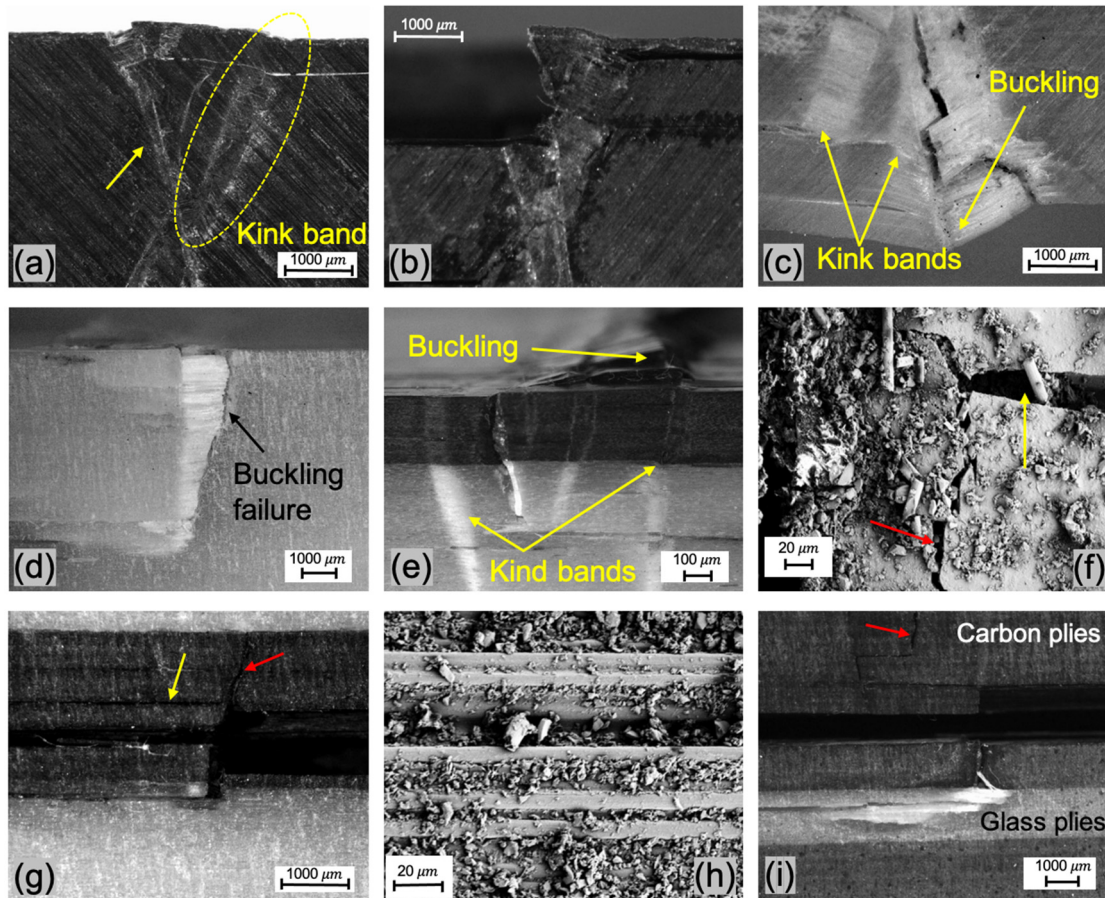
Fig. 4. (a) Optical micrograph showing formation of kink bands on the compressive side of AC specimen, (b) Optical micrograph of AC specimen showing the compressive failure due to carbon fiber buckling, (c) Optical micrograph of AG specimen showing multiple kink bands formation and buckling of glass fibers on the compressive side, (d) Optical micrograph of buckling failure in AG specimen in the thickness direction, (e) Optical micrograph of buckling failure, and extension of kink bands across carbon and glass plies though the thickness in 1C specimen, (f) SEM micrograph of 1C specimen showing transverse crack growth in matrix (red arrow) and onset of delamination failure (yellow arrow), (g) Optical micrograph of 2C specimen showing transverse crack in carbon fiber plies (red arrow) and delamination failure interfaces (yellow arrow), (h) SEM micrograph of 3C laminate showing extensive shear-driven delamination failure in carbon fiber plies along the horizontal midplane, (i) Optical micrograph of 13C specimen showing transverse crack formation in carbon fiber plies (red arrow) and delamination failure along the horizontal midplane. (For interpretation of the colors in the figure(s), the reader is referred to the web version of this article.)

in Fig. 3(b). Moreover, flexural strength of AC and 13C laminates is strongly correlated with their exhibited brittle damage mechanisms, even though they contain the highest amounts of carbon fibers as compared to other hybrid/non-hybrid laminates. In fact, the failure initiation in carbon fibers poses a critical limitation in terms of controlling the strength of hybrid laminates. More importantly, after the hybridization effect of glass fibers, the flexural strength of the AC specimen immensely improves such that being even larger than its intrinsic strength property. This improvement results from the efficient stress redistribution in hybrid specimens due to the presence of high-elongation glass fibers, and the generation of hybrid effect, which prevents the premature failure observed for the all-carbon specimen [55].

Under flexural loading condition, the laminate experiences compressive, tensile, and shear stresses through the thickness direction. In the area under the loading tip during a flexural test, a high concentration of compressive stresses is present, which triggers fiber micro-buckling (or kinking) along with matrix yielding [56,57]. These kink band formations can be clearly observed in both non-hybrid specimens (AC and AG) at multiple places, as shown in Fig. 4(a–d). After the onset of transverse cracks, once the broken in-plane fibers are unable to provide reinforcement through the thickness of the laminate, the material depends on the remaining intact plies to carry the load. Moreover, in addition to the low through-the-thickness strength, the high interlaminar

shear stresses generated within the pristine plies cause delamination failures in bending specimens. That is why delamination failure mode was observed for all specimens. However, in the AG specimen, right before delamination occurrence, matrix yielding together with fiber micro-buckling was inspected. Later, the accumulation of high compressive stresses resulted in the creation of a crack tip, which propagated in the form of a delamination failure in AG laminate. Overall, in both non-hybrid specimens, extensive buckling due to different levels of compressive stresses was the initial failure mode at the top plies.

Remarkably, AC specimens failed as a result of highly unpredictable deformation mechanisms. By scrutinizing microscopic results and inspection of the failed samples with a naked eye, it can be suggested that two different failure paths are feasible for AC laminates. The first method of failure in AC laminates shows a growth of a profound transverse crack through the thickness from the top layer followed by delamination at plies closer to the midplane of the specimen, where shear stresses are more significant. The second path for failure in AC specimens does not reveal severe damage at the top layers due to compressive failure, but a rather abrupt interlaminar delamination in the midplane of the samples due to induced in-plane shear loading. Thus, there is an unpredictability in the failure development mechanism in AC composites. Nonetheless, although failure of hybrid samples is more dynamic due to the presence of brittle layers with varying stiff-

ness values; after interply fiber hybridization of AC noticeable predictability in the failure modes was achieved, especially in the 1C, 2C, and 3C hybrid laminates as discussed hereafter.

In the hybrid specimens, the kink band formation at the top layer was more prominent in specimens containing carbon plies on the faces i.e., in 1C and 13C, as shown in Fig. 4(e) and Fig. 4(i), respectively, due to the low compressive strength of carbon fibers. In a unidirectional laminate under a flexural load, the compressive stress varies linearly through the thickness [58]. Therefore, a compressive failure triggered by fiber micro-buckling resulted in the formation of a transverse crack at the top carbon layers of 1C and 13C specimens, later propagating in a direction parallel to the loading axis. This crack transformed into delamination failure as a result of very high interlaminar shear stress [59]. As shown in Fig. 4(a), the first drop at the stress in the stress–strain curve of 1C laminate is related to buckling of the top surface. The further stress drops observed for the 1C specimen are likely to be related to the growth and propagation of kink band damage towards the middle layers. An additional splitting tensile failure in the bottom layers occurred in the 1C specimen, as the transverse strain values reached an excess of +1.13%. The analogous stepwise decrease in material stiffness was observed in 13C laminate. The first drop is correlated with compressive damage due to kink band formation on the top carbon layers, which later propagated through the glass layers beneath them. Afterward, delamination is observed at multiple interfaces along the carbon plies parallel to the horizontal midplane, and in the carbon/glass interface at the tensile side of 13C specimen as shown in Fig. 4(i). However, the dominant failure modes were compressive failure and shear-driven delamination along the fiber direction.

In the 2C laminate, although the maximum load level was unable to initiate macro compressive failure in the top glass layers, the carbon plies next to them suffered from a transverse crack formation as seen in Fig. 4(g). The resultant crack tip generation in carbon plies ultimately caused instantaneous delamination failure in the fiber direction at the glass/carbon interfaces correlating with the sudden stress drop in the stress–strain curve of the 2C specimen.

A highly brittle instantaneous failure behavior was also exhibited by the 3C laminate and a stepwise drop in the stress levels could not be observed in the stress–strain curve. Remarkably, delamination failure was initiated from the free edges by creating a fracture surface along the fiber direction in the 3C specimen. Moreover, as the carbon fibers located along the midplane have a higher modulus, the critical strain energy release rate needed to initiate delamination in carbon fibers is much lower compared to glass fibers [60,61]. Thus, a premature shear-driven interlaminar delamination failure was exhibited by 3C specimen along horizontal midplane, separating the specimens into two halves as seen in (Fig. 4h).

The comparison of flexural stress versus flexural strain curves for 1C, 2C, and 3C thick samples in current investigation with previously studied thin counterparts [21] indicates that the flexural modulus reduces as the carbon layers are placed closer to the midplane of the hybrid laminate regardless of their thickness. Although the flexural strength increases for thin 1C, 2C, and 3C laminates in the given order [21], the thick 2C laminate shows the highest average strength in the current investigation, and the thick 3C laminate has the lowest average failure strains as depicted in Fig. 3(b). Since microscopic images of both thin [21] and thick 2C (see Fig. 4g) laminates show transverse crack at top layers further developed via interlaminar delamination, it can be concluded that such an anomaly is not due to variation of damage growth in 2C laminate but a change in the failure mode of thick 2C specimen. As shown in Fig. 4(h), failure for 3C specimen appears as midplane delamination while no damage is observed in middle carbon layers for thin

3C specimen [21]. Hence, the thickness increase for middle carbon layers reduces the flexural strength of 3C sample despite providing a higher failure strain as compared to the AC laminate. As seen in Fig. 3(a), the thick 13C specimen shows an abrupt single step failure, while the thin 13C laminate reveals stepwise drops in the stress due to damage progress [21]. The stepwise stress drops in thin laminate are attributed to buckling of surface carbon layers followed by shear-driven transverse crack in middle carbon plies. However, the progress of failure to middle layers is not observed for thick samples as seen in Fig. 4(i). Thus, it is evident that the failure of thick carbon layers at the surface is not further developed as a shear-driven transverse crack in the middle layers of the laminate, and unlike the thin 13C specimen, the failure strain of the thick laminate is controlled by surface layers rather than through the thickness plies.

As seen in Fig. 4(e) and observed in the previous study [21], both thick and thin laminates with 1C stacking sequence show kink bands formed at surface carbon layers and their growth towards glass layers beneath. While the development of crack is stopped for thin 1C sample at the midplane, it continues as interlaminar delamination for the thick specimen as seen in Fig. 4(e). This behavior can be attributed to the presence of significant in-plane shear stresses at the midplane of the thick specimen, which contribute to further development of the failure as delamination and consequent increase in failure strain in the thick specimen as compared to its thin counterpart. Overall, it is evident that size effect can change failure progress in interply fiber hybrid laminates which can be analyzed via damage monitoring techniques such as AE analysis.

The explained failure mechanisms for the thick hybrid samples were reproducible, hence it can be implied that replacing carbon layers in AC laminate with glass fiber plies can contribute to the predictability of failure path under flexural loading condition. This information can be used efficiently for shape sensing approaches such as iFEM-RZT [62,63] and to identify the susceptible locations for failure in hybrid fiber laminates while implementing SHM techniques such as active sensing methods [64].

3.2. Full field strain measurements using DIC

DIC technique was used to obtain technical strain fields developed in unidirectional specimens at 25%, 50%, 75%, and 100% of the ultimate flexural strength ($\sigma_{ultimate}$) during the 3-point bending tests. The results are presented in Figs. 6-8. For the DIC analysis of the transverse strain (ε_{xx}) and shear strain (ε_{xy}), the area under the loading tip is chosen, as it has the highest localization of applied load due to the specific design of a bending test. This area is named as the region of interest (ROI) and is shown in Fig. 5.

The distribution of transverse strains and shear strain for the non-hybrid specimens is shown in Fig. 6(a–b) and Fig. 6(c–d), respectively. The results in Fig. 6(a) indicate a highly localized longitudinal strain profile developing in the AC laminate at the maximum flexural strength ($\sigma_{ultimate}$) in a direction parallel to the loading axis. The concentrated compressive strain extends through the thickness of the specimen reaching a maximum value of −2.42% and correlates well with the observed crack tip in the failed specimen. In comparison, as shown in Fig. 6(b), the ε_{xx} profile in the AG specimen is symmetric, with a homogeneous distribution of compressive strain on the top and tensile strain at the bottom of the specimen under maximum load. The high ductility of glass fibers prevents axial splitting at the bottom of the specimen, allowing it to reach a high ε_{xx} value of +2.49%. As seen in Fig. 6(c), the ε_{xy} strain field shows a concentration at $\sigma_{ultimate}$ orienting parallel to the loading direction (crack formation direction) in the AC specimen, and in the lower half, it orients itself parallel to the fiber direction. The highly concentrated narrow band profile of shear
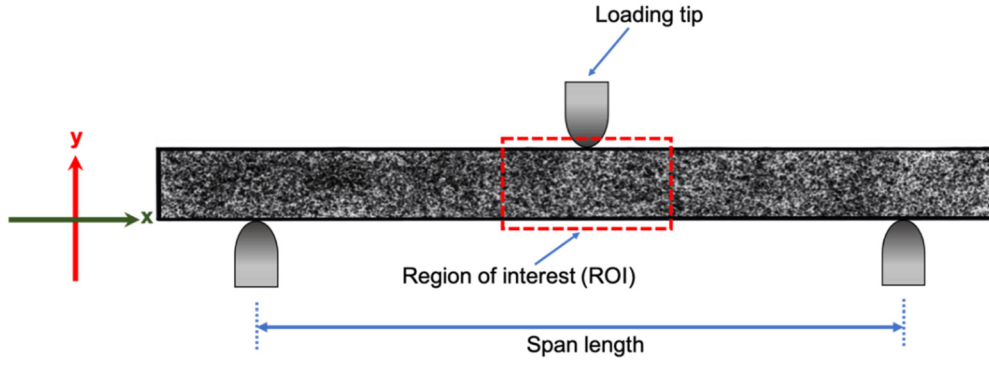
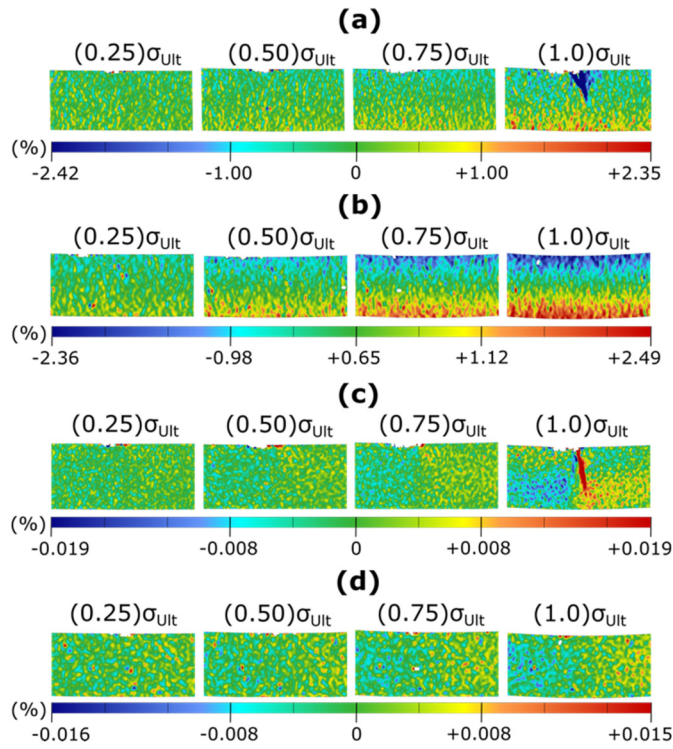**Fig. 5.** Region of interest (ROI) under the loading tip chosen for strain field analysis using DIC.

Fig. 6. 2D-DIC technical strain fields at 25%, 50%, 75% and 100% of ultimate flexural strength (a) ε_{xx} (transverse strain) fields of AC specimen, (b) ε_{xx} (transverse strain) fields of AG specimen, (c) ε_{xy} (shear strain) fields of AC specimen and (d) ε_{xy} (shear strain) fields of AG specimen.

Fig. 7. 2D-DIC through-thickness transverse strain (ε_{xx}) fields at 25%, 50%, 75% and 100% of ultimate flexural strength for (a) 1C specimen, (b) 2C specimen, (c) 3C specimen and (d) 13C specimen.

strain combined with an existing transverse strain results in the formation of a delamination failure path in the AC specimen in the lower plies. In other words, the development of a crack parallel to the loading direction results in the creation of an extra shear strain field at the right side of the failed region as seen in for AC laminate at $\sigma_{ultimate}$, consequently inducing interlaminar delamination at perpendicular to the loading axis. Fig. 6(d) exhibits the ε_{xy} field of the AG specimen at various stress values. It can be observed that even at the maximum load level, the shear strain in the specimen is significantly diffused as compared to that of AC specimen and is positioned parallel to the horizontal midplane.

Fig. 7(a–d) depicts DIC results in terms of transverse strain plots in the region of interest for all hybrid laminates at different stress levels. As seen in Fig. 7(a), ε_{xx} in the form of localized bands parallel to the loading direction has appeared in the bottom plies of 1C laminate during the linear elastic stage of the test. As the applied load increases, the tensile strain redistributes itself parallel to the bottom carbon layers, and a concentrated compressive strain has
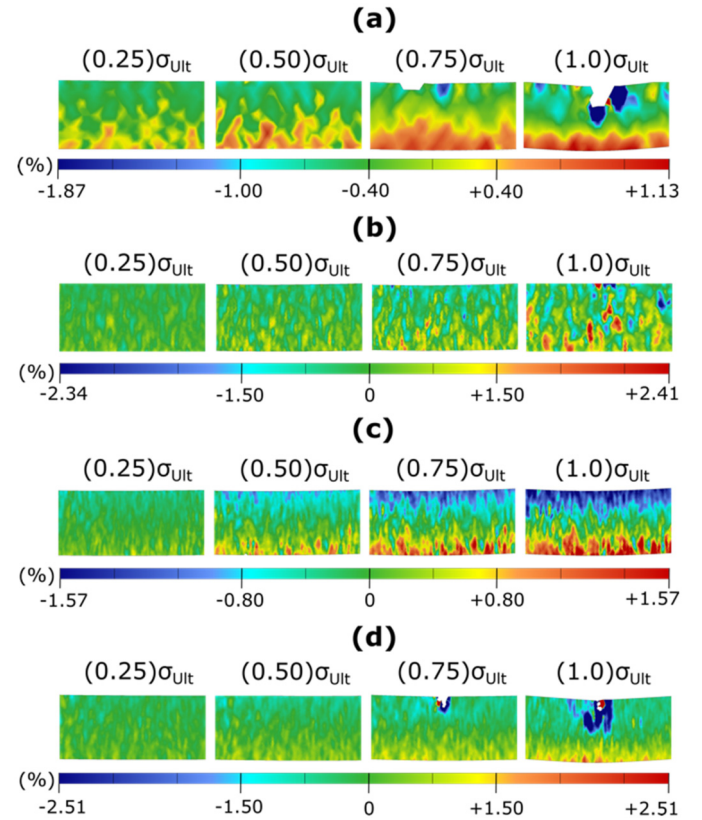
also appeared at 75% of the maximum load. The high strain concentration in the top carbon layers results in the formation of a crack tip that propagates downwards, parallel to the loading axis. As the plies located towards the bottom of specimen are no longer able to sustain the high compressive stresses, the crack tip extends in the form of delamination failure in the 1C specimen. Moreover, as the ultimate strength value approaches, the tensile stresses generated in bottom layers due to ε_{xx} being above +1.13%, cause axial splitting of the bottom plies. In the 2C specimen, the presence of glass plies on the compressive and tensile side allows the laminate to sustain a higher strain value before failing.

It can be observed in Fig. 7(b) that the concentration of transverse strain is positioned parallel to the loading direction in the 2C laminate in form of narrow bands and results in transverse crack formation in carbon layers, as shown in Fig. 4(g). However, the inhomogeneity of strain fields in the 2C specimen may be at-
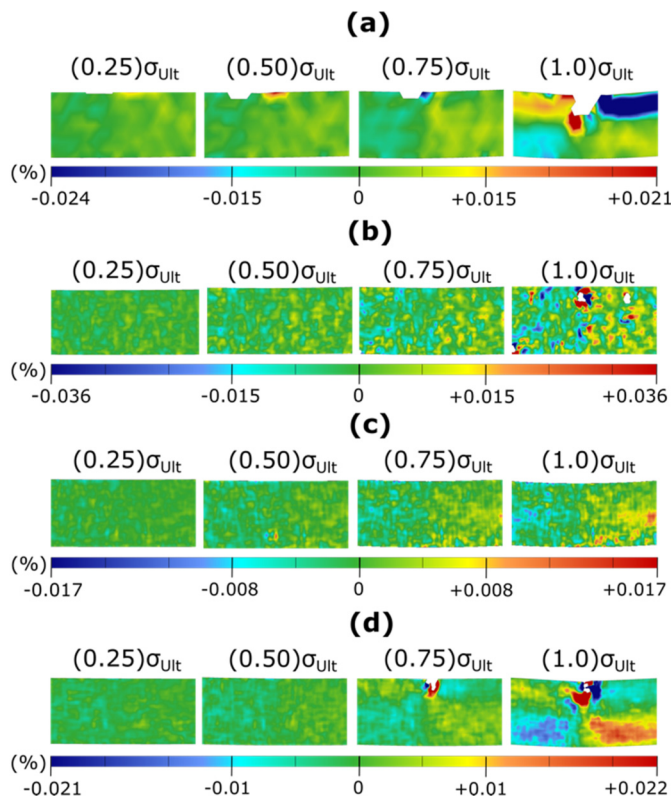
Fig. 8. 2D-DIC through-thickness shear strain (ε_{xy}) fields at 25%, 50%, 75% and 100% of ultimate flexural strength for (a) 1C specimen, (b) 2C specimen, (c) 3C specimen and (d) 13C specimen.

tributed to random surface defects. Fig. 7(c) shows the transverse strain maps for the 3C specimen. It can be observed that similar to the AG specimen, the distribution of longitudinal strain is symmetric about the horizontal midplane and is mainly concentrated along the glass plies. The high ductility and low stiffness of glass fibers prevent possible stress accumulation and impede the formation of a macro crack tip.

As discussed earlier, among the hybrid specimens, extensive crack formation due to compressive stresses was only observed in specimens with carbon plies on the faces. Therefore, as shown in Fig. 7(d), similar to the AC and 1C specimen, a relatively saturated compressive transverse strain up to −2.5% can be seen in the 13C specimen appearing at 75% of the maximum strength. The resulting transverse crack later reaches the carbon plies located along the horizontal midplane of the specimen and converts later into a delamination failure mode.

Fig. 8(a–d) presents the DIC results for shear strain fields at various stress levels in the hybrid specimens in the area under the loading tip during the bending tests. For all the specimens the generation of shear strain at 50% of ultimate strength is negligible.

Fig. 8(a) and Fig. 8(d) show an extensive shear strain concentration along the fiber direction for both 1C and 13C specimens. Although the maximum ε_{xy} values for both laminates are comparable i.e., +0.021%, the location of strain concentration varies, and correlates well with the shear-driven failure observed in top plies in the 1C laminate, and along the middle in the 13C laminate. A more heterogeneous shear strain distribution is observed for 2C laminate, as shown in Fig. 8(b). The inhomogeneity of shear strain field accumulation through the thickness of 2C resulted in the formation of multiple delamination paths along the fiber direction. As seen in Fig. 8(c), the shear strain in 3C laminate has also accumulated along the carbon plies in the middle of the specimen along the horizontal midplane. As discussed in earlier sections, the

delamination failure in 3C laminate started from the free-edges, and the presence of highly localized shear strain bands, away from the vertical midplane explains such delamination onset. Notice the nearly zero ε_{xy} under the loading tip in the 3C laminate in Fig. 8(c) which indicates minimal transverse crack initiation under the loading tip during the test.

3.3. Damage accumulation during bending tests

Fig. 9 provides the clustering results for acoustic emission data of bending tests for the AC and AG composite specimens. In these graphs of PP1 vs WPF, three clusters with distinguishable frequency ranges can be observed for the specimens i.e., 45–180 kHz, 180–350 kHz, and 350–550 kHz, referred to as fc_1, fc_2, and fc_3, respectively. The fc_1 range is attributed to cracking in the resin matrix [65], therefore, in all the recorded AE data, the lowest frequency range of WPF is due to damage initiation or its propagation in the resin matrix. The remaining two frequency ranges are consequently related to other damage types manifested by the laminates under mechanical loading. The intermittent frequency range (fc_2) is, therefore, associated with the fiber/matrix interface failure or delamination, as defined previously in the literature [10,66]. Even though in the hybrid laminates, two fiber types are present, but a previous study conducted by authors confirms that both carbon and glass fibers break at the highest frequency range [21]. So, the fc_3 range corresponds to the fiber breakage for all specimens under bending load [67].

Fig. 10 presents the results of stress–strain curves obtained from the bending test apparatus (UTM) and DIC results with cumulative counts of acoustic emission hits. Strain values for DIC curves are calculated according to the ASTM D790-A standard using local displacement of a selected point on the specimen surface during bending tests, while stress values are obtained from the load-cell data. Fig. 10(a–f) reveal that the initial damages registered in the specimens by the AE equipment are related to the highest frequency damage i.e., fiber breakage. Due to the specific set-up of a 3-point bending test, micro-buckling or breakage of fibers at the compressive side of the specimens is usually the preliminary damage type, which is observed well in Fig. 10 for all non-hybrid and hybrid laminates. A similar result for the initial damage type for thin hybrid laminates with the same stacking sequence was observed in [21].

The acoustic emission activity for AC and AG started at flexural strain levels of 1.09% and 1.30%, respectively. As seen in Fig. 10(a), for the AC laminate, all three damage types accumulate and increase by several orders of magnitude as the material approaches failure strain, resulting in a spontaneous catastrophic failure. It is interesting to note that for AC, at the first instant of stiffness degradation which corresponds to a visible stress drop, no AE data is recorded. It might be due to fact that the amplitude of acoustic waves generated at this instance falls below the sensitivity threshold of the AE sensor. In Fig. 10(b), as soon as the experimental data deviate from the DIC results (dashed lines), AE activity starts for the AG specimen. As DIC is measuring real-time displacement fields at cross-section of the specimen, it can capture the stiffness loss very efficiently for the AG specimen. However, similar to the AC specimen, an exponential increase in acoustic emission activity was recorded for AG before the global failure of the specimen albeit with a small slope at the final stage.

For the hybrid specimens, the start of AE activity was recorded for strain levels less than 0.95%. For the 1C specimen, a very dynamic failure behavior was observed, with a stepwise drop in material stiffness under the bending load. As seen in Fig. 10(c), the concurrent start of matrix cracking, interface failure, and fiber breakage is observed. This conforms with fractography results obtained for 1C specimen showing transverse crack generation in the
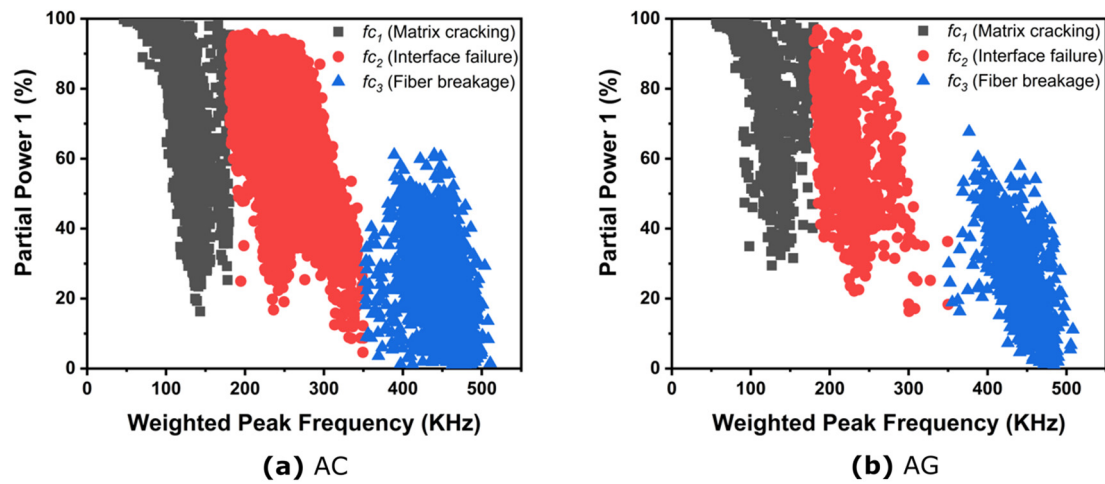
(a) AC   **(b)** AG

Fig. 9. Sample clustering results of acoustic emission data for composite specimens during 3-point bending tests.

resin, as well as the onset of interface debonding from Fig. 4(f). As shown in Fig. 10(d), for the 2C specimen, the DIC stress–strain curve was able to capture the start of stiffness loss in the laminate. Fiber breakage and matrix cracking start at the same moment, followed by fiber/matrix debonding in 2C. Unlike the abrupt rise in counts value observed in the non-hybrid specimens, a steady increase in AE count is observed for this specimen which can be attributed to the transverse cracking in the 2C sample as observed in transverse strain plots shown for DIC images (Fig. 7b) and captured in the optical micrographs in Fig. 4(g). It is also observed that cumulative counts values for interface failure in 2C laminate undergo a steady increase until global failure, suggesting multiple delamination path generations in the specimen with the increase in mechanical load.

Among all hybrid specimens, the lowest AE counts for interface failure were recorded for the 3C specimen as shown in Fig. 10(e). This observation is consistent with the abrupt growth of interlaminar delamination in the middle layers of this sample. Moreover, for the 3C specimen, AE data suggest the occurrence of fiber damage inside the specimen, which could not be captured by the optical-based DIC system. Fig. 10(f) shows the evolution of AE counts for 13C specimen under flexural loading. Fiber breakage and matrix cracking were the two damage forms registered initially by the AE system, increasing in count spontaneously as the nonlinear region in stress–strain curve approaches. This correlates well with the transverse crack generation observed in 13C laminate due to high compressive stress in the top carbon layers. However, after an abrupt increase, the AE activities stabilize and continue to rise with a steady slope until the global failure of the specimen.

Fig. 10(f) shows that the AE activity starts when the DIC stress–strain curve deviates from the experimental results, capturing loss of flexural modulus. The analysis of acoustic emission activity for AC and the hybrid specimens reveals that after fiber hybridization of AC with glass fiber, the damage initiation and propagation behavior of hybrid specimens under flexural loading can be altered significantly. In other words, as a result of interply fiber hybridization damage accumulation rate becomes gradual for hybrid samples as compared to abrupt failure growth in AC laminate. This type of steady failure growth implies that hybrid laminates are better candidates for continuous structural health monitoring under quasi-static loading conditions. It is also noted that for all hybrid laminates, the strain levels for which acoustic activity starts are lower than that of AG specimen, suggesting that the presence of stiff carbon plies is dominating the damage initiation. Moreover, it is observed that once the macro damage has initiated inside the hybrid laminates, glass plies are no longer able to arrest it.

Table 3
Acoustic emission hit fraction for various damage types in composite laminates.

Sample	Hit fraction (%)		
	Matrix cracking	Interface failure	Fiber breakage
AC	49	24	27
AG	48	29	23
1C	37	6	58
2C	53	8	39
3C	55	5	38
13C	31	10	60

Table 3 summarizes the hit fraction percentage related to various damage types for all the specimens. When compared to the AG specimen, damage accumulation due to fiber breakage in AC is higher. However, it can also be observed that the hybrid specimens are more prone to fiber micro-damage accumulation compared to the non-hybrid specimens. This effect may be attributed to the presence of two fiber types in hybrid laminates which intensifies the loading conditions due to the introduction of transverse shear stresses in material as per a previous study by the authors [21]. Moreover, the hit fraction percentage for interface failure in hybrid laminates is significantly lower as compared to both AC and AG laminates.

4. Conclusions

An experimental study to investigate the mechanical behavior and failure modes of thick hybrid composites laminates under bending load is performed by using two different SHM and/or non-destructive testing methods, i.e., digital image correlation technique and acoustic emission method. The bending tests performed on thick hybrid laminates reveal that the selected stacking sequence has an apparent correlation with flexural properties and failure mechanisms exhibited by the specimens. The flexural modulus of hybrid laminates is mainly controlled by the location of high stiffness fiber plies. The closer these plies to the bounding faces of the laminate are, the higher the flexural modulus is. Flexural strength, however, is mostly controlled by the mode of damage initiation and its subsequent propagation within the thick composite laminates. It is found out that the fiber hybridization of carbon laminate with glass fibers can improve its flexural strength, as observed in the 2C and 13C hybrid specimens. In addition, an experimental solution concerning failure unpredictability in thick carbon fiber laminates is suggested. It is revealed that in all the hybrid laminates, depending on a particular stacking sequence, similar and anticipated global failure modes are exhibited. This
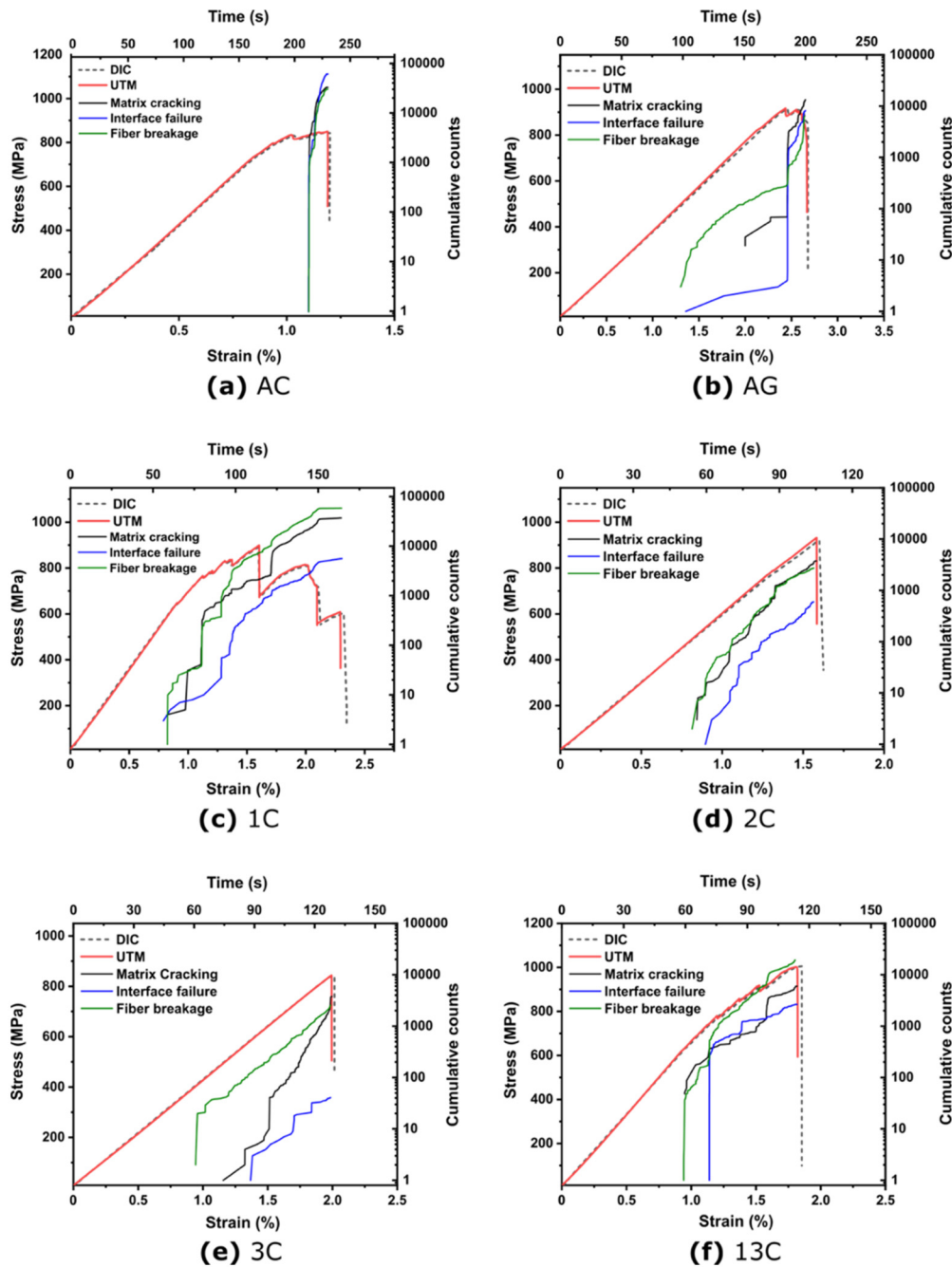
Fig. 10. Combined plots of stress–strain curves and Acoustic Emission cumulative count-time plots for composite laminates during flexural tests.

predictability can be used for shape sensing and NDE inspection of thick hybrid fiber laminates.

The fractography of failed non-hybrid and hybrid laminates suggests that the final failure mode in all thick laminates under flexural loading is extensive shear-driven delamination along the fiber direction. Moreover, damage initiation in hybrid laminates always occurs in the high stiffness carbon fiber plies, either in the form of transverse micro-crack generation or fiber/matrix debonding. Furthermore, as compared to the thin hybrid laminates studied in [21], the mechanical performance and damage behavior of thick hybrid laminates under flexural loading conditions is obviously different due to the size effect. As such, the higher the thickness of hybrid laminate, the easier the growth of interlaminar delamination within the plies, thereby leading to a reduction in flexural strength of thick hybrid laminates. It is demonstrated that such a size effect may need to be considered for effective selection of

glass layer locations through the thickness of the thick hybrid laminates for increasing their structural strength.

The digital image correlation technique is used to monitor the through-thickness evolution of transverse and shear strains in the laminates. It is demonstrated that laminates with high stiffness plies on the faces exhibit localized strain concentration underneath the loading tip during the flexural tests. However, laminates with ductile fiber plies on the faces, do not exhibit such strain accumulation, due to successful dissipation of stress by the glass fibers through the thickness of the laminates. DIC technique can be effectively used to monitor the transverse as well as shear strain variation along the thickness direction and to predict the strain values corresponding to damage onset in hybrid laminates.

Acoustic emission analysis of the recorded data indicates the presence of three weighted peak frequency ranges attributed to three different failure types occurring in the laminates. These fail-

ure types are matrix cracking, fiber/matrix interface failure, and fiber breakage, corresponding to frequency ranges of 45–180 kHz, 180–350 kHz, and 350–550 kHz, respectively. The cumulative counts versus time curves suggest that various damage modes in the hybrid laminates accumulate gradually during mechanical loading, unlike in the carbon laminate, where the recorded acoustic emission activity is instantaneous, and global failure occurs without any prior warning. Moreover, it is noted that in the hybrid laminates, AE hit fraction related to high-frequency damage (i.e., fiber breakage) increases as compared to the non-hybrid laminates. The strain levels where AE activity starts in the hybrid laminates is found to be associated with the fiber-breakage of high-stiffness carbon fibers.

Declaration of competing interest

The authors declare that they have no known competing financial interests or personal relationships that could have appeared to influence the work reported in this paper.

Acknowledgement

References

[1] H. Mainka, O. Täger, E. Körner, L. Hilfert, S. Busse, F.T. Edelmann, A.S. Herrmann, Lignin – an alternative precursor for sustainable and cost-effective automotive carbon fiber, J. Mater. Res. Technol. 4 (2015) 283–296, https://doi.org/10.1016/j.jmrt.2015.03.004.

[2] Boeing: 787 By Design: Advanced Composite Use (n.d.), https://www.boeing.com/commercial/787/by-design/#/advanced-composite-use. (Accessed 15 January 2021).

[3] J. Watanabe, F. Tanaka, R. Higuchi, H. Matsutani, H. Okuda, T. Okabe, A study of stress concentrations around fiber breaks in unidirectional CF/epoxy composites using double-fiber fragmentation tests, Adv. Compos. Mater. 27 (2018) 575–587, https://doi.org/10.1080/09243046.2017.1416567.

[4] C. Elanchezhian, B.V. Ramnath, J. Hemalatha, Mechanical behaviour of glass and carbon fibre reinforced composites at varying strain rates and temperatures, Proc. Mater. Sci. 6 (2014) 1405–1418, https://doi.org/10.1016/j.mspro.2014.07.120.

[5] A. Viglietti, E. Zappino, E. Carrera, Free vibration analysis of variable angle-tow composite wing structures, Aerosp. Sci. Technol. 92 (2019) 114–125, https://doi.org/10.1016/j.ast.2019.05.068.

[6] G.G. Lozano, A. Tiwari, C. Turner, S. Astwood, A review on design for manufacture of variable stiffness composite laminates, Proc. Inst. Mech. Eng., B J. Eng. Manuf. 230 (2016) 981–992, https://doi.org/10.1177/0954405415600012.

[7] T.H. Hsieh, A.J. Kinloch, K. Masania, J. Sohn Lee, A.C. Taylor, S. Sprenger, The toughness of epoxy polymers and fibre composites modified with rubber microparticles and silica nanoparticles, J. Mater. Sci. 45 (2010) 1193–1210, https://doi.org/10.1007/s10853-009-4064-9.

[8] D.W.Y. Wong, L. Lin, P.T. McGrail, T. Peijs, P.J. Hogg, Improved fracture toughness of carbon fibre/epoxy composite laminates using dissolvable thermoplastic fibres, Composites, Part A, Appl. Sci. Manuf. 41 (2010) 759–767, https://doi.org/10.1016/j.compositesa.2010.02.008.

[9] K.L. Kepple, G.P. Sanborn, P.A. Lacasse, K.M. Gruenberg, W.J. Ready, Improved fracture toughness of carbon fiber composite functionalized with multi walled carbon nanotubes, Carbon 46 (2008) 2026–2033, https://doi.org/10.1016/j.carbon.2008.08.010.

[10] B. AlKhateab, I.E. Tabrizi, J.S.M. Zanjani, M.N. Rahimi, L.H. Poudeh, A. Kefal, M. Yildiz, Damage mechanisms in CFRP/HNT laminates under flexural and in-plane shear loadings using experimental and numerical methods, Composites, Part A, Appl. Sci. Manuf. 136 (2020) 105962, https://doi.org/10.1016/j.compositesa.2020.105962.

[11] P.N. Khanam, H.P.S.A. Khalil, M. Jawaid, G.R. Reddy, C.S. Narayana, S.V. Naidu, Sisal/carbon fibre reinforced hybrid composites: tensile, flexural and chemical resistance properties, J. Polym. Environ. 18 (2010) 727–733, https://doi.org/10.1007/s10924-010-0210-3.

[12] H.N. Dhakal, Z.Y. Zhang, R. Guthrie, J. MacMullen, N. Bennett, Development of flax/carbon fibre hybrid composites for enhanced properties, Carbohydr. Polym. 96 (2013) 1–8, https://doi.org/10.1016/j.carbpol.2013.03.074.

[13] H.A. Aisyah, M.T. Paridah, S.M. Sapuan, A. Khalina, O.B. Berkalp, S.H. Lee, C.H. Lee, N.M. Nurazzi, N. Ramli, M.S. Wahab, R.A. Ilyas, Thermal properties of woven kenaf/carbon fibre-reinforced epoxy hybrid composite panels, Int. J. Polym. Sci. 2019 (2019), https://doi.org/10.1155/2019/5258621.

[14] A.R. Bunsell, B. Harris, Hybrid carbon and glass fibre composites, Composites 5 (1974) 157–164, https://doi.org/10.1016/0010-4361(74)90107-4.

[15] T.D. Jagannatha, G. Harish, Mechanical properties of carbon/glass fiber reinforced epoxy hybrid polymer composites, Int. J. Mech. Eng. Rob. Res. 4 (2015) 131–137.

[16] T. Hayashi, On the improvement of mechanical properties of composites by hybrid composition, in: Proc. 8th Intl. Reinforced Plast. Conf., 1972, pp. 149–152, http://ci.nii.ac.jp/naid/10004555738/en/.

[17] Y. Swolfs, R.M. McMeeking, I. Verpoest, L. Gorbatikh, The effect of fibre dispersion on initial failure strain and cluster development in unidirectional carbon/glass hybrid composites, Composites, Part A, Appl. Sci. Manuf. 69 (2015) 279–287, https://doi.org/10.1016/j.compositesa.2014.12.001.

[18] M.V. Mousavi, H. Khoramishad, The effect of hybridization on high-velocity impact response of carbon fiber-reinforced polymer composites using finite element modeling, Taguchi method and artificial neural network, Aerosp. Sci. Technol. 94 (2019) 105393, https://doi.org/10.1016/j.ast.2019.105393.

[19] C. Dong, I.J. Davies, Optimal design for the flexural behaviour of glass and carbon fibre reinforced polymer hybrid composites, Mater. Des. 37 (2012) 450–457, https://doi.org/10.1016/j.matdes.2012.01.021.

[20] R.K. Prusty, D.K. Rathore, B.P. Singh, S.C. Mohanty, K.K. Mahato, B.C. Ray, Experimental optimization of flexural behaviour through inter-ply fibre hybridization in FRP composite, Constr. Build. Mater. 118 (2016) 327–336, https://doi.org/10.1016/j.conbuildmat.2016.05.054.

[21] I.E. Tabrizi, A. Kefal, J.S.M. Zanjani, C. Akalin, M. Yildiz, Experimental and numerical investigation on fracture behavior of glass/carbon fiber hybrid composites using acoustic emission method and refined zigzag theory, Compos. Struct. 223 (2019) 110971, https://doi.org/10.1016/j.compstruct.2019.110971.

[22] A. Fahr, B. Roge, M. Brothers, D.G. Zimcik, Inspection of thick composites for near surface flaws, Sci. Eng. Compos. Mater. 11 (2004) 177–183, https://doi.org/10.1515/secm.2004.11.2-3.177.

[23] M.E. Ibrahim, Nondestructive evaluation of thick-section composites and sandwich structures: a review, Composites, Part A, Appl. Sci. Manuf. 64 (2014) 36–48, https://doi.org/10.1016/j.compositesa.2014.04.010.

[24] T.E. Twardowski, S.E. Lin, P.H. Geil, Curing in thick composite laminates: experiment and simulation, J. Compos. Mater. 27 (1993) 216–250, https://doi.org/10.1177/002199839302700301.

[25] A. Djabali, L. Toubal, R. Zitoune, S. Rechak, Fatigue damage evolution in thick composite laminates: combination of X-ray tomography, acoustic emission and digital image correlation, Compos. Sci. Technol. 183 (2019) 107815, https://doi.org/10.1016/j.compscitech.2019.107815.

[26] J. Lee, C. Soutis, A study on the compressive strength of thick carbon fibre-epoxy laminates, Compos. Sci. Technol. 67 (2007) 2015–2026, https://doi.org/10.1016/j.compscitech.2006.12.001.

[27] W.L. Cheng, S. Langlie, S. Itoh, High velocity impact of thick composites, Int. J. Impact Eng. (2003) 167–184, https://doi.org/10.1016/j.ijimpeng.2003.09.015.

[28] S.E. Boyd, T.A. Bogetti, J.M. Staniszewski, B.D. Lawrence, M.S. Walter, Enhanced delamination resistance of thick-section glass-epoxy composite laminates using compliant thermoplastic polyurethane interlayers, Compos. Struct. 189 (2018) 184–191, https://doi.org/10.1016/j.compstruct.2018.01.062.

[29] X. Gao, B. Sun, B. Gu, Damage mechanisms of 3-D rectangular braided composite under multiple impact compressions, Aerosp. Sci. Technol. 82–83 (2018) 46–60, https://doi.org/10.1016/j.ast.2018.08.031.

[30] H. Hamidi, W. Xiong, S.V. Hoa, R. Ganesan, Fatigue behavior of thick composite laminates under flexural loading, Compos. Struct. 200 (2018) 277–289, https://doi.org/10.1016/j.compstruct.2018.05.149.

[31] A. Gorjipoor, S. Van Hoa, R. Ganesan, Numerical model for investigation of the strain distribution in thick composite plates subjected to bolt loads, Aerosp. Sci. Technol. 59 (2016) 94–102, https://doi.org/10.1016/j.ast.2016.10.008.

[32] S.C. Khatri, M.J. Koczak, Thick-section AS4-graphite/E-glass/PPS hybrid composites: part II. Flexural response, Compos. Sci. Technol. 56 (1996) 473–482, https://doi.org/10.1016/0266-3538(96)00002-4.

[33] R. Roy, M. Gherlone, C. Surace, A shape sensing methodology for beams with generic cross-sections: application to airfoil beams, Aerosp. Sci. Technol. 110 (2021) 106484, https://doi.org/10.1016/j.ast.2020.106484.

[34] M. Esposito, M. Gherlone, Composite wing box deformed-shape reconstruction based on measured strains: optimization and comparison of existing approaches, Aerosp. Sci. Technol. 99 (2020) 105758, https://doi.org/10.1016/j.ast.2020.105758.

[35] W.H. Peters, W.F. Ranson, M.A. Sutton, T.C. Chu, J. Anderson, Application of digital correlation methods to rigid body mechanics, Opt. Eng. 22 (1983) 73–76, https://doi.org/10.1117/12.7973231.

[36] W.H. Peters, W.F. Ranson, Digital imaging techniques in experimental stress analysis, Opt. Eng. 21 (1982) 213427, https://doi.org/10.1117/12.7972925.

[37] A. Pagani, R. Azzara, E. Carrera, E. Zappino, Static and dynamic testing of a full-composite VLA by using digital image correlation and output-only ground vibration testing, Aerosp. Sci. Technol. 112 (2021) 106632, https://doi.org/10.1016/j.ast.2021.106632.

[38] M. Grédiac, The use of full-field measurement methods in composite material characterization: interest and limitations, Compos. Part A Appl. Sci. Manuf. 35 (2004) 751–761, https://doi.org/10.1016/j.compositesa.2004.01.019.

[39] T. Hua, H. Xie, S. Wang, Z. Hu, P. Chen, Q. Zhang, Evaluation of the quality of a speckle pattern in the digital image correlation method by mean subset fluctuation, Opt. Laser Technol. 43 (2011) 9–13, https://doi.org/10.1016/j.optlastec.2010.04.010.

[40] J. Bohse, Acoustic emission characteristics of micro-failure processes in polymer blends and composites, Compos. Sci. Technol. 60 (2000) 1213–1226, https://doi.org/10.1016/s0266-3538(00)00060-9.

[41] S. Barré, M.L. Benzeggagh, On the use of acoustic emission to investigate damage mechanisms in glass-fibre-reinforced polypropylene, Compos. Sci. Technol. 52 (1994) 369–376, https://doi.org/10.1016/0266-3538(94)90171-6.

[42] J.M. Berthelot, J. Rhazi, Acoustic emission in carbon fibre composites, Compos. Sci. Technol. 37 (1990) 411–428, https://doi.org/10.1016/0266-3538(90)90012-T.

[43] J. Cuadra, P.A. Vanniamparambil, K. Hazeli, I. Bartoli, A. Kontsos, Damage quantification in polymer composites using a hybrid NDT approach, Compos. Sci. Technol. 83 (2013) 11–21, https://doi.org/10.1016/j.compscitech.2013.04.013.

[44] C. Yilmaz, C. Akalin, I. Gunal, H. Celik, M. Buyuk, A. Suleman, M. Yildiz, A hybrid damage assessment for E- and S-glass reinforced laminated composite structures under in-plane shear loading, Compos. Struct. 186 (2018) 347–354, https://doi.org/10.1016/j.compstruct.2017.12.023.

[45] J. Jefferson Andrew, V. Arumugam, D.J. Bull, H.N. Dhakal, Residual strength and damage characterization of repaired glass/epoxy composite laminates using A.E. and D.I.C, Compos. Struct. 152 (2016) 124–139, https://doi.org/10.1016/j.compstruct.2016.05.005.

[46] F.E. Oz, N. Ersoy, M. Mehdikhani, S.V. Lomov, Multi-instrument in-situ damage monitoring in quasi-isotropic CFRP laminates under tension, Compos. Struct. 196 (2018) 163–180, https://doi.org/10.1016/j.compstruct.2018.05.006.

[47] C. Goidescu, H. Welemane, C. Garnier, M. Fazzini, R. Brault, E. Péronnet, S. Mistou, Damage investigation in CFRP composites using full-field measurement techniques: combination of digital image stereo-correlation, infrared thermography and X-ray tomography, https://doi.org/10.1016/j.compositesb.2012.11.016, 2012.

[48] F.E. Oz, N. Ersoy, S.V. Lomov, Do high frequency acoustic emission events always represent fibre failure in CFRP laminates?, Composites, Part A, Appl. Sci. Manuf. 103 (2017) 230–235, https://doi.org/10.1016/j.compositesa.2017.10.013.

[49] H.Q. Ali, I. Emami Tabrizi, R.M.A. Khan, A. Tufani, M. Yildiz, Microscopic analysis of failure in woven carbon fabric laminates coupled with digital image correlation and acoustic emission, Compos. Struct. 230 (2019) 111515, https://doi.org/10.1016/j.compstruct.2019.111515.

[50] ASTM D790-17, Standard test methods for flexural properties of unreinforced and reinforced plastics and electrical insulating materials, 2017.

[51] M.G.R. Sause, T. Müller, A. Horoschenkoff, S. Horn, Quantification of failure mechanisms in mode-I loading of fiber reinforced plastics utilizing acoustic emission analysis, Compos. Sci. Technol. 72 (2012) 167–174, https://doi.org/10.1016/j.compscitech.2011.10.013.

[52] M. Kempf, O. Skrabala, V. Altstädt, Acoustic emission analysis for characterisation of damage mechanisms in fibre reinforced thermosetting polyurethane and epoxy, Composites, Part B, Eng. 56 (2014) 477–483, https://doi.org/10.1016/j.compositesb.2013.08.080.

[53] C. Sellitti, S. Vargui, E. Martuscelli, D. Fabbro, Wettability of glass fibres with different sizings and their adhesion to unsaturated polyester matrices, J. Mater. Sci. 22 (1987) 3477–3484, https://doi.org/10.1007/BF01161445.

[54] G. Suresh, L.S. Jayakumari, Evaluating the mechanical properties of E-Glass fiber/carbon fiber reinforced interpenetrating polymer networks, Polimeros 25 (2015) 49–57, https://doi.org/10.1590/0104-1428.1650.

[55] G. Czél, M. Jalalvand, M.R. Wisnom, Demonstration of pseudo-ductility in unidirectional hybrid composites made of discontinuous carbon/epoxy and continuous glass/epoxy plies, Composites, Part A, Appl. Sci. Manuf. 72 (2015) 75–84, https://doi.org/10.1016/j.compositesa.2015.01.019.

[56] S. Kyriakides, R. Arseculeratne, E.J. Perry, K.M. Liechti, On the compressive failure of fiber reinforced composites, Int. J. Solids Struct. 32 (1995) 689–738, https://doi.org/10.1016/0020-7683(94)00157-R.

[57] H.M. Jensen, J. Christoffersen, Kink band formation in fiber reinforced materials, J. Mech. Phys. Solids 45 (1997) 1121–1136, https://doi.org/10.1016/S0022-5096(96)00126-3.

[58] I.M. Daniel, H.M. Hsiao, S.C. Wooh, Failure mechanisms in thick composites under compressive loading, Composites, Part B, Eng. 27 (1996) 543–552, https://doi.org/10.1016/1359-8368(95)00010-0.

[59] M.R. Wisnom, The role of delamination in failure of fibre-reinforced composites, Philos. Trans. R. Soc., Math. Phys. Eng. Sci. 370 (2012) 1850–1870, https://doi.org/10.1098/rsta.2011.0441.

[60] L. Lagunegrand, T. Lorriot, R. Harry, H. Wargnier, J.M. Quenisset, Initiation of free-edge delamination in composite laminates, Compos. Sci. Technol. 66 (2006) 1315–1327, https://doi.org/10.1016/j.compscitech.2005.10.010.

[61] A.K. El-Senussi, J.P.H. Webber, Critical strain energy release rate during delamination of carbon fibre reinforced plastic laminates, Composites 20 (1989) 249–256, https://doi.org/10.1016/0010-4361(89)90340-6.

[62] A. Kefal, I.E. Tabrizi, M. Yildiz, A. Tessler, A smoothed iFEM approach for efficient shape-sensing applications: Numerical and experimental validation on composite structures, Mech. Syst. Signal Process. 152 (2021) 107486, https://doi.org/10.1016/j.ymssp.2020.107486.

[63] A. Kefal, I.E. Tabrizi, M. Tansan, E. Kisa, M. Yildiz, An experimental implementation of inverse finite element method for real-time shape and strain sensing of composite and sandwich structures, Compos. Struct. 258 (2021) 113431, https://doi.org/10.1016/j.compstruct.2020.113431.

[64] D. Gao, Z. Wu, L. Yang, Y. Zheng, W. Yin, Structural health monitoring for long-term aircraft storage tanks under cryogenic temperature, Aerosp. Sci. Technol. 92 (2019) 881–891, https://doi.org/10.1016/j.ast.2019.02.045.

[65] C. Yilmaz, M. Yildiz, A study on correlating reduction in Poisson's ratio with transverse crack and delamination through acoustic emission signals, Polym. Test. 63 (2017) 47–53, https://doi.org/10.1016/j.polymertesting.2017.08.001.

[66] P.J. de Groot, P.A.M. Wijnen, R.B.F. Janssen, Real-time frequency determination of acoustic emission for different fracture mechanisms in carbon/epoxy composites, Compos. Sci. Technol. 55 (1995) 405–412, https://doi.org/10.1016/0266-3538(95)00121-2.

[67] R.M.A. Khan, I.E. Tabrizi, H.Q. Ali, E. Demir, M. Yildiz, Investigation on interlaminar delamination tendency of multidirectional carbon fiber composites, Polym. Test. 90 (2020) 106653, https://doi.org/10.1016/j.polymertesting.2020.106653.